



OPEN

SUBJECT AREAS:

BATTERIES

POLYMERS

Received

1 November 2013

Accepted

17 March 2014

Published

8 April 2014

Correspondence and requests for materials should be addressed to S.-Y.L. (syleek@unist.ac.kr)

Multifunctional semi-interpenetrating polymer network-nanoencapsulated cathode materials for high-performance lithium-ion batteries

Ju-Myung Kim¹, Jang-Hoon Park¹, Chang Kee Lee² & Sang-Young Lee¹

¹Interdisciplinary School of Green Energy, Ulsan National Institute of Science and Technology (UNIST), Ulsan 689-798, Korea, ²Korea Packaging Center, Korea Institute of Industrial Technology, Bucheon, Gyeonggi-do 421-742, Korea.

As a promising power source to boost up advent of next-generation ubiquitous era, high-energy density lithium-ion batteries with reliable electrochemical properties are urgently requested. Development of the advanced lithium ion-batteries, however, is staggering with thorny problems of performance deterioration and safety failures. This formidable challenge is highly concerned with electrochemical/thermal instability at electrode material-liquid electrolyte interface, in addition to structural/chemical deficiency of major cell components. Herein, as a new concept of surface engineering to address the abovementioned interfacial issue, multifunctional conformal nanoencapsulating layer based on semi-interpenetrating polymer network (semi-IPN) is presented. This unusual semi-IPN nanoencapsulating layer is composed of thermally-cured polyimide (PI) and polyvinyl pyrrolidone (PVP) bearing Lewis basic site. Owing to the combined effects of morphological uniqueness and chemical functionality (scavenging hydrofluoric acid that poses as a critical threat to trigger unwanted side reactions), the PI/PVP semi-IPN nanoencapsulated-cathode materials enable significant improvement in electrochemical performance and thermal stability of lithium-ion batteries.

With the advent of rapidly growing industrial fields such as smart mobile electronics, electric vehicles, and grid-scale energy storage systems, high-energy density lithium-ion rechargeable batteries with reliable electrochemical attributes are highly requested as a promising power source^{1,2}. Development of the advanced lithium ion-batteries, however, is staggering with thorny issues of performance deterioration and safety problems, which are concerned with their complex physicochemical/electrochemical phenomena between major components (such as cathodes, anodes, electrolytes, and separator membranes). Notably, these formidable interfacial issues become more pronounced at high-voltage cell approach, which is spotlighted as an effective way to improve energy density (=voltage [V] x coulomb capacity [C]) of cells^{3,4}. Raising the charge cut-off voltage above a conventional value, however, may give rise to serious concerns associated with capacity loss during charge/discharge cycling and also safety failure, which are believed to mainly arise from unwanted side reactions at cathode-electrolyte interface⁵⁻⁹. In this respect, there is no doubt that understanding and control of interfacial phenomena between cathode materials and liquid electrolytes are needed as an essential prerequisite for developing high-energy density/high-safety cells.

Among various research approaches to manipulate cathode-electrolyte interface, surface modification of cathode materials with inorganic materials (e.g. Al₂O₃, ZrO₂, and AlF₃) has been extensively investigated¹⁰⁻¹², along with synthesis of new cathode materials and electrolytes showing well-fledged electrochemical properties. The advantageous effects of inorganic coatings, however, are shadowed by discontinuous deposition of inorganic materials, poor ionic/electronic conduction, and also complex/cost-consuming manufacturing processes.

In addition to the inorganic coatings, electron conducting polymers-based surface modification of cathode materials has also garnered a great deal of attention due to their good electronic conductivity and easy processability. Poly(3,4-ethylenedioxythiophene) (PEDOT) was exploited as a coating material to enhance surface electronic conductivity of LiFePO₄ cathode materials, which thus exerted beneficial influence on rate capability of cells incorporating the PEDOT-coated LiFePO₄^{13,14}. Unique function of 3-hexylthiophene as a polymerizable, life-extending additive was demonstrated, where the addition of 3-hexylthiophene into ethylene carbonate (EC)/



dimethyl carbonate (DMC)-based liquid electrolyte improves cycling performance of high capacity $\text{Li}_{1.2}\text{Ni}_{0.15}\text{Co}_{0.1}\text{Mn}_{0.55}\text{O}_2$ and high voltage $\text{LiNi}_{0.5}\text{Mn}_{1.5}\text{O}_4$ cathodes¹⁵.

Different from the abovementioned inorganic and electron conducting polymer-based coatings, our group recently reported a new surface modification strategy based on ion-conductive polymer thin layer, where thermally-cured polyimide (PI) was chosen as a kind of soft matter-based coating material^{16–18}. However, a large portion of cathode material surface still remains intact without being covered by PI coating layer. Moreover, the PI coating layer does not contain any chemical functional groups that may mitigate undesirable interfacial side reaction between cathode materials and liquid electrolyte.

In this study, as a new concept of structural design and interface control strategy, multifunctional conformal nanoencapsulating layer based on semi-interpenetrating polymer network (semi-IPN) is presented. Semi-IPN, which is characterized by well-designed heterogeneous phase structure composed of chemically-crosslinked polymer and linear chain polymer, is known to be a simple and efficient material engineering that can easily tailor structural/physicochemical characteristics of final polymer products for a wide variety of applications^{19,20}. Here, poly(vinyl pyrrolidone) (PVP) bearing Lewis basic site^{21,22} is chosen and combined with PI to adjust polarity of resulting PI/PVP semi-IPN, which plays a viable role in constructing conformal nanoencapsulating layer with large surface coverage on cathode materials. In addition to this morphological uniqueness, pyrrolidone rings of PVP are expected to scavenge hydrofluoric acid (HF), which is inevitably generated by side reactions between water impurities and lithium salts such as LiPF_6 in liquid electrolytes. Because the HF is considered as a critical threat to trigger harmful side reactions in cells, elimination of HF in liquid electrolytes is strongly demanded to secure excellent cell performance^{8,23}. Thus, the PVP exploited herein is likely to act as HF-scavenging polymeric additive as well as polarity-tuning agent for PI/PVP semi-IPN-nanoencapsulated cathode materials.

Based on the characterization of morphological/chemical uniqueness of PI/PVP semi-IPN nanoencapsulating layer, its influence on cell performance and thermal stability of high voltage-charged cathode materials is investigated and also discussed with an in-depth analysis of electrochemical behavior/structural variation of electrode materials during charge/discharge cycling. The present study demonstrates that the conformal PI/PVP semi-IPN nanoencapsulating layer featuring the unique multifunctionality is effective in overcoming the interfacial challenges between electrode materials and liquid electrolytes and thus can be suggested as a new class of surface engineering to boost development of advanced lithium-ion electrode materials.

Results

Synthesis and structural/physicochemical characterization of PI/PVP-semi-IPN nanoencapsulated LCO. The PVP is mixed with pyromellitic dianhydride (PMDA)/oxydianiline (ODA)-based polyamic acid copolymer (=PI precursor) (Figure S1), wherein the composition ratio of polyamic acid/PVP is fixed at 50/50 w/w. Variation in composition ratio of polyamic acid/PVP and its influence on structure/electrochemical characteristics of PI/PVP semi-IPN nanoencapsulating layer will be investigated in future studies. The polyamic acid/PVP mixtures are subjected to thermal imidization under the presence of cathode materials (here, LiCoO_2 (LCO) powders are chosen as a model system), leading to the formation of PI/PVP semi-IPN nanoencapsulating layer on LCO surface (hereinafter, denoted as “PI/PVP-LCO”). The surface morphology of PI/PVP-LCO was characterized and compared with those of single component-coated LCO (i.e., PI- and PVP-LCO), with a focus on coverage area of LCO surface. Figure 1a shows that the PI/PVP-LCO has highly-continuous and conformal polymeric layers on LCO surface. In comparison, for the PI-LCO, relatively large portion of LCO surface remains intact without being coated

with the PI layer (Figure S2a). Meanwhile, for the PVP-LCO, randomly scattered dot-like PVP domains are formed on LCO surface (Figure S2b). The highly-continuous conformal morphology of the PI/PVP nanoencapsulating layer was further elucidated by conducting TEM characterization (an inset image of Figure 1b). It is apparent that the LCO is covered with ultrathin, conformal PI/PVP film (thickness ~ 10 nm). The thickness of PI/PVP nanoencapsulating layer is believed to depend on polymer concentration in the polyamic acid/PVP coating solution (dimethylacetamide (DMAc) is used as a solvent). Here, the polymer concentration in the coating solution was fixed at 0.5 wt%. More detailed investigation on the thickness control of nanoencapsulating layer and its influence on cell performance will be an intriguing research topic of our subsequent studies.

The successful formation of PI/PVP nanoencapsulating layer with large surface coverage is also confirmed with TOF-SIMS mapping images (Figure 1c). For the PI/PVP-LCO (left side of Figure 1c), the red dots assigned to C-N bonds of the PI/PVP semi-IPN are uniformly dispersed over a wide area of LCO surface and few yellow dots corresponding to Co elements are detected, indicating that the LCO surface is well covered with the PI/PVP encapsulating layer. By contrast, the pristine LCO (right side of Figure 1c) shows high concentration of Co elements and no detectable level of C-N bonds. Meanwhile, the XRD patterns (Figure S3) exhibit no significant difference between the pristine LCO and PI/PVP-LCO, both of which show typical layered structure of hexagonal $\alpha\text{-NaFeO}_2$ type with $R\bar{3}m$ space group²⁴. This XRD result reveals that the introduction of PI/PVP nanoencapsulating layer does not disrupt the layered crystalline structure of bulk LCO.

To attain a better understanding of the PI/PVP nanoencapsulating layer, its phase separation behavior was scrutinized. Unfortunately, direct characterization of the PI/PVP-LCO did not provide meaningful results, probably due to the extremely small amount of PI/PVP coating layer. Instead, as supplementary experiment, a self-standing PI/PVP film (thickness ~ 15 μm) was prepared and its phase separation behavior was analyzed. The DSC profiles (Figure 1d) show that the PI/PVP semi-IPN has two different T_g s ($\sim 200^\circ\text{C}$ for PVP, $\sim 290^\circ\text{C}$ for PI), indicating the evolution of phase-separated structure. This phase-separated structure of PI/PVP semi-IPN was also evidenced by analyzing its FT-IR peaks (Figure 1e). The PI/PVP semi-IPN exhibits three characteristic FT-IR peaks at 1425, 1675, and 1723 cm^{-1} , which respectively correspond to C-N, C=O bonds of PVP, and C=O bonds of PI^{25,26}. In other words, with respect to the FT-IR peaks of single component PI or PVP, no appreciable peak shift was observed at the PI/PVP semi-IPN, proving that PI and PVP are phase separated in the PI/PVP semi-IPN.

To further elucidate this intriguing phase separation behavior, the morphology (cross-sectional view) of PI/PVP semi-IPN film was analyzed. Prior to the FE-SEM measurement, the PVP phase in the PI/PVP semi-IPN film was selectively etched using DMAc solvent ($80^\circ\text{C}/12$ h). It is evident that highly-developed porous structure is formed in the PI/PVP semi-IPN film (Figure S4). Using the same etching process, the morphological variation of PI/PVP-LCO was examined. In comparison to the relatively smooth and even coating layer before the etching (an inset image of Figure 1b), the rough and bumpy coating layer was observed after the etching (Figure 1b), demonstrating the selective removal of PVP phase. This result is a good evidence to prove the nanoscale phase-separated structure in the PI/PVP coating layer on LCO surface.

The polarity of polymers used herein (i.e., PI, PVP, and PI/PVP), which is believed to exert significant influence on morphological evolution of coating layer on LCO surface, was investigated by measuring their water contact angle. Figure 1f shows that the water contact angle of the PI/PVP film is approximately 47° , which is a value between those of the PI ($\sim 96^\circ$) and PVP film ($\sim 17^\circ$). This result exhibits that the semi-IPN architecture composed of polar PVP

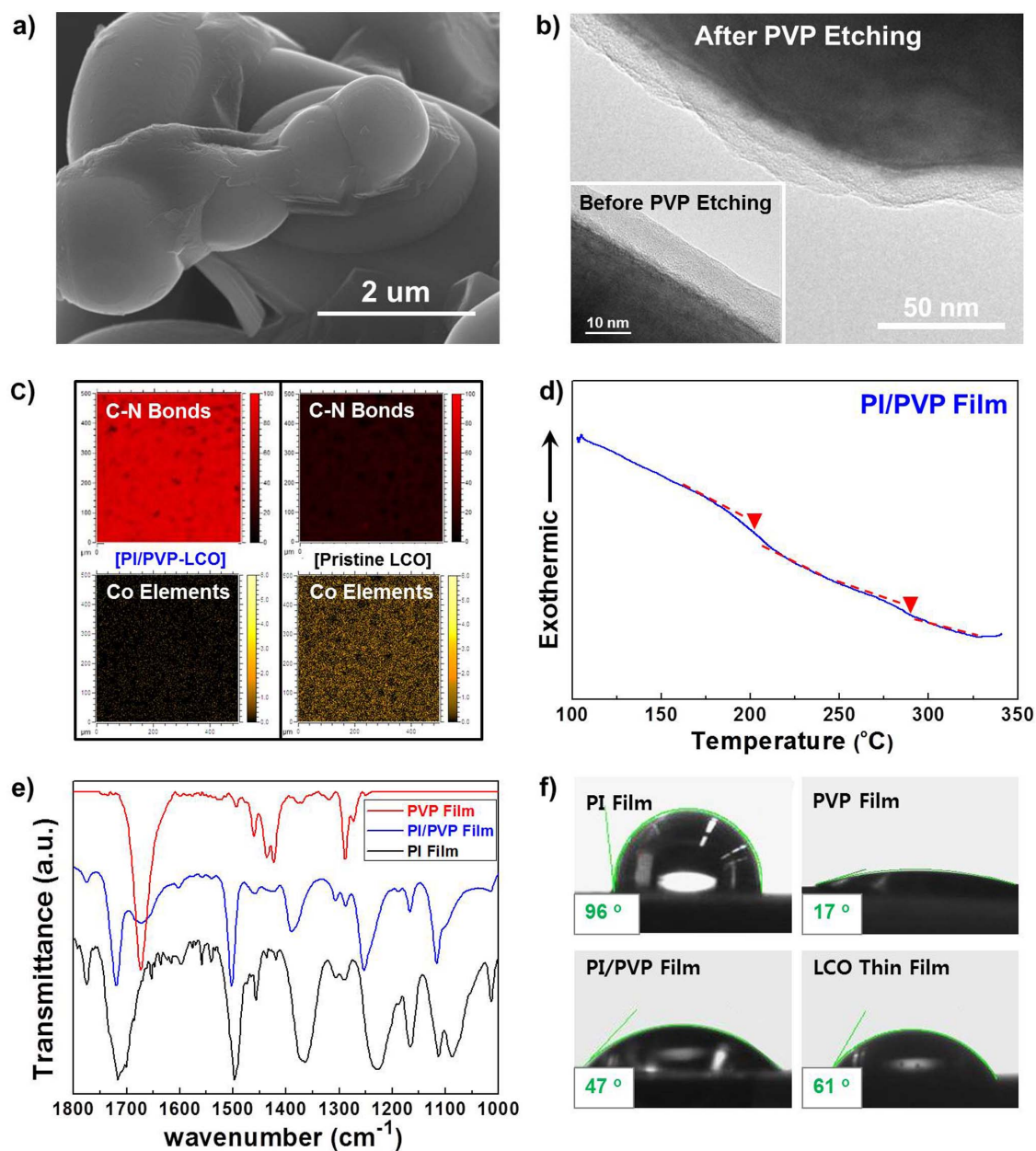


Figure 1 | Structural characterization of PI/PVP-LCO. (a) FE-SEM photograph; (b) TEM photographs before/after selective etching of PVP phase; (c) TOF-SIMS mapping images (red dots = C-N bonds and yellow dots = Co elements). Phase separation behavior of PI/PVP semi-IPN film: (d) DSC profile showing two different glass transition temperatures (T_g); (e) FT-IR spectra (characteristic peaks at 1425 (C-N bonds of PVP), 1675 (C=O bonds of PVP), and 1723 cm^{-1} (C=O bonds of PI)). (f) Water contact angle of PI, PVP, PI/PVP film, and LCO thin film.

and less-polar PI is an efficient way to tune the polarity of resulting polymer products. Meanwhile, to estimate water contact angle of LCO, LCO thin film, which was supplied from GS nanotech (Korea), was used, because a self-standing/dense-structured LCO film was very difficult to obtain with LCO powders. The water contact angle of LCO thin film is observed to be 61° . The comparison of these water contact angle data demonstrates that the polarity of the PI/PVP semi-IPN is well-matched with that of the LCO thin film (i.e., smallest gap in water contact angle ($14^\circ = 61^\circ$ (LCO thin film) - 47° (PI/PVP film)), as compared to those of the PI and PVP. This is a good evidence to support the morphological uniqueness of conformal PI/PVP nanoencapsulating layer with large surface coverage on LCO.

Effect of PI/PVP-semi-IPN nanoencapsulated LCO on electrochemical performance/thermal stability of high-voltage charged cells. Based on the abovementioned understanding of morphological

uniqueness and phase separation behavior, effect of PI/PVP-LCO on high-voltage cell performance was investigated. Figure 2a shows cycling performance (i.e., discharge capacity retention as a function of cycle number) of cells at a constant charge/discharge current density ($=0.5 \text{ C}/0.5 \text{ C}$). At a high-voltage charge condition (here, 4.4 V was chosen as a representative voltage), the discharge capacity of pristine LCO tends to sharply decrease with cycling. This poor performance may be ascribed to the unwanted interfacial side reaction between the charged LCO and liquid electrolyte. It is known that, at high voltage conditions, conventional carbonate-based liquid electrolytes are vulnerable to electrochemical decomposition on delithiated LCO surface, yielding harmful resistive layers that may hamper charge transfer across LCO surface during cycling⁸⁻¹¹.

Meanwhile, negligible level of improvement in the cycling performance was found at the PVP-LCO, indicating that the poorly-developed

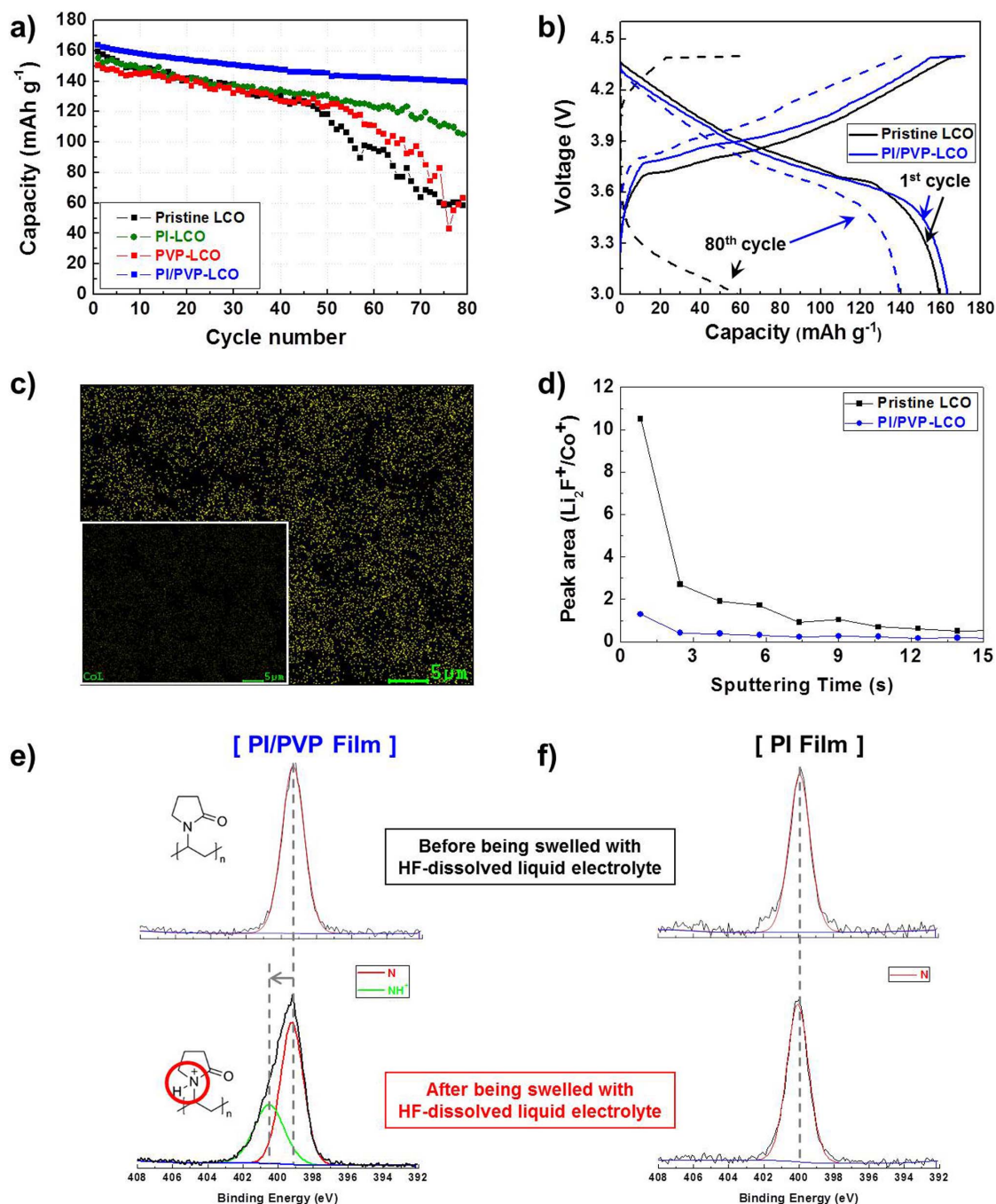


Figure 2 | High-voltage cell performance. (a) comparison of cycling performance between pristine LCO, PI-LCO, PVP-LCO, and PI/PVP-LCO (charge/discharge current density = 0.5 C/0.5 C); (b) charge/discharge profiles of pristine LCO and PI/PVP-LCO (charge/discharge current density = 0.5 C/0.5 C). Compositional change of electrode surface after 80th cycle: (c) EDS images showing cobalt elements (represented by yellow dots) deposited on anode surface for a cell incorporating pristine LCO (inset image is for PI/PVP-LCO); (d) TOF-SIMS depth profile of Li₂F⁺ concentration on LCO surface (pristine LCO vs. PI/PVP-LCO). Variation in XPS spectra (characteristic peak of nitrogen (N) atoms) of PI/PVP or PI film after being swelled with HF (100 ppm)-dissolved liquid electrolyte (1 M LiPF₆ in EC/EMC = 1/2 v/v): (e) PI/PVP film; (f) PI film.

PVP coating layer (i.e., randomly scattered dot-like domains) does not mitigate the interfacial side reaction although PVP has Lewis basic site. On the other hand, the PI-LCO presents the better cycling performance than the pristine and PVP-LCO. Notably, the most stable capacity retention was observed at the PI/PVP-LCO. After 80th cycle, the capacity retention is 85% for the PI/PVP-LCO, as compared to those of pristine LCO (~38%), PVP-LCO (~42%), and PI-LCO (~68%). This superior capacity retention of the PI/PVP-LCO was further evidenced by the small increase in ohmic polarization after 80th cycle (from the charge/discharge profiles

shown in Figure 2b). The abovementioned analysis of cycling performance demonstrates that the PI/PVP nanoencapsulating layer with large surface coverage effectively protects LCO surface from the attack of violent liquid electrolyte, thereby suppressing the unwanted interfacial side reactions. Meanwhile, the cycling performance at a charge cut-off voltage of 4.2 V (charge/discharge current density = 0.5 C/0.5 C), which has been widely used in commercial lithium-ion batteries, was also measured (Figure S5). No significant difference was observed between the pristine LCO and PI/PVP-LCO at this mild charging condition.

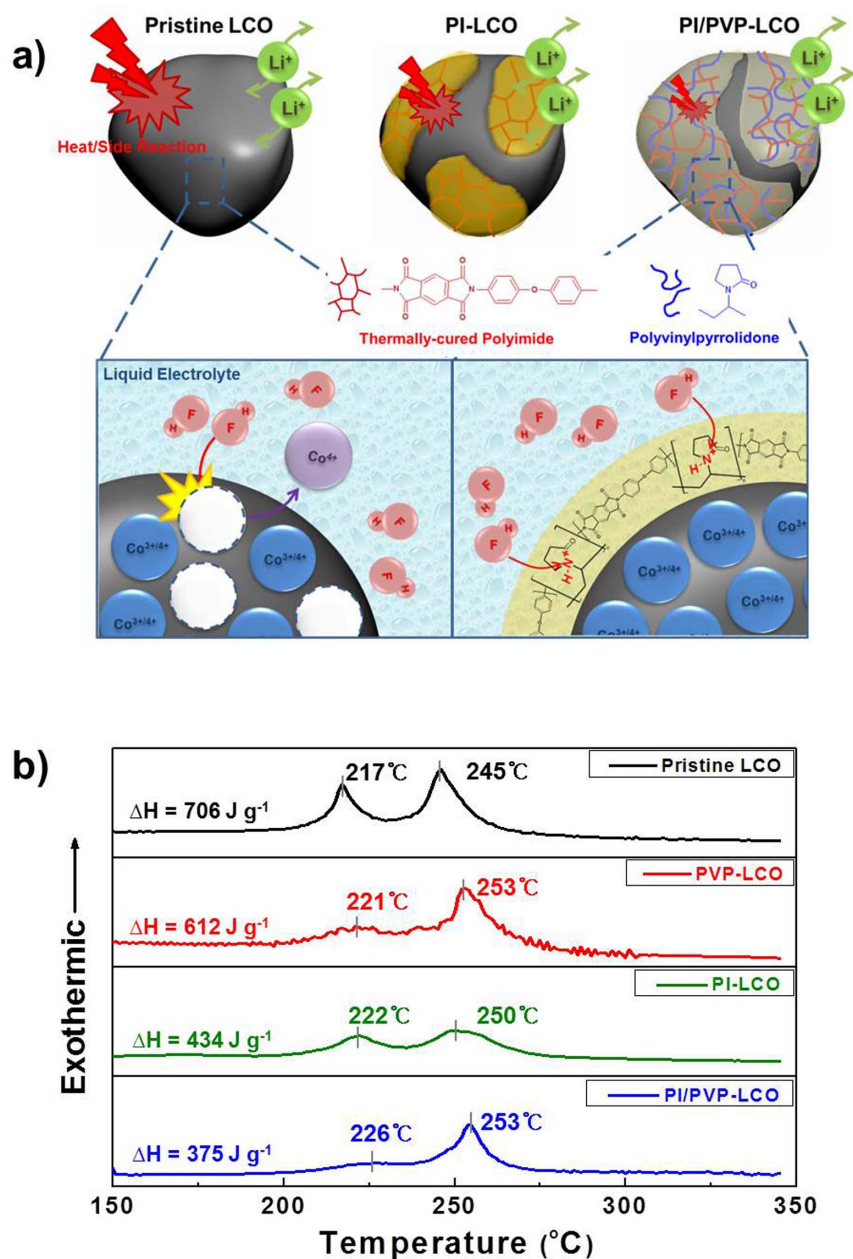


Figure 3 | (a) A conceptual illustration depicting multifunctional benefits of PI/PVP nanoencapsulating layer on the interfacial stability between delithiated LCO and liquid electrolyte as an ion-conductive protective conformal layer. (b) DSC thermograms showing interfacial exothermic reaction between delithiated LCO (pristine LCO, PI-LCO, PVP-LCO, and PI/PVP-LCO) and liquid electrolyte.

To understand ionic transport through the PI/PVP nanoencapsulating layer, ionic conductivity of a self-standing, liquid electrolyte (1 M LiPF₆ in EC/EMC = 1/2 v/v)-swollen PI/PVP film was measured as a supplementary experiment. From the analysis of Cole-Cole plot (Figure S6), the ionic conductivity was estimated to be 0.36 mS cm⁻¹ at room temperature. Thus, it is reasonably expected that the liquid electrolyte-swollen, nanometer-thick PI/PVP coating layer allows facile ionic transport, contributing to negligibly impairing charge transfer kinetics between the LCO and bulk liquid electrolyte. This favorable ionic transport via the PI/PVP encapsulating layer also exerts a beneficial influence on discharge C-rate capability of the PI/PVP-LCO (Figure S7). No significant difference in discharge capacity was observed between the pristine LCO and PI/PVP-LCO over a wide range of discharge current density varying from 0.2 to 2.0 C.

The unusual cycling performance of the PI/PVP-LCO was explained by analyzing the AC impedance spectra of 4.4 V-charged cells after 80th cycle (Figure S8a). The growth of cell impedance after 80th cycle is considerably retarded at the PI/PVP-LCO ($Z_{Re}(80^{th} \text{ cycle}) - Z_{Re}(1^{st} \text{ cycle}) = \Delta Z_{Re} \sim 80 \text{ ohm}$), as compared to pristine LCO ($\Delta Z_{Re} \sim 650 \text{ ohm}$). In addition, the variation in electrode polarization during cycling was examined using cyclic voltammetry (Figure S8b). After 80th cycle, the PI/PVP-LCO shows the smaller potential difference between anodic and cathodic peak ($\Delta V \sim 0.55 \text{ V}$), as compared to the pristine LCO ($\Delta V \sim 1.17 \text{ V}$). The aforementioned electrochemical analysis verifies that the PI/PVP nanoencapsulating layer effectively suppresses the unwanted interfacial side reactions between LCO and liquid electrolyte, thereby suppressing the formation of unwanted resistive layers²⁷ that hamper charge transfer kinetics.



The advantageous effect of PI/PVP nanoencapsulating layer on the cycling performance was further confirmed by observing the compositional change of electrode surface. The EDS image (Figure 2c) shows that, for the cell containing the pristine LCO, after 80th cycle, the anode surface is seriously contaminated with large numbers of impurities mainly assigned to cobalt compounds (represented by yellow dots). Previous studies^{28,29} reported that cobalt dissolution from delithiated LCO, which tends to be triggered by HF present in liquid electrolytes, results in cobalt deposition on anode surface via ionic migration in liquid electrolytes. By contrast, for a cell assembled with the PI/PVP-LCO, inappreciable amount of cobalt compounds are detected on the anode surface (inset image of Figure 2c).

This beneficial contribution of the PI/PVP nanoencapsulating layer was also quantitatively elucidated by measuring Co⁺ ions on the anode surface and also Li₂F⁺ content on the LCO surface using TOF-SIMS characterization. Consistent with the morphological results, the amount of Co⁺ deposited on the anode surface is considerably decreased at the PI/PVP-LCO (Figure S9). Figure 2d depicts the TOF-SIMS depth profile of Li₂F⁺ concentration on LCO surface. The smaller amount of Li₂F⁺, one of byproducts generated from HF-driven decomposition of LiPF₆ salts in liquid electrolytes^{8,9,30}, is deposited on the PI/PVP-LCO, as compared to the pristine LCO. The EDS and TOF-SIMS results underline the advantageous effect of PI/PVP nanoencapsulating layer on suppressing interfacial side reaction between LCO and liquid electrolyte.

The pyrrolidone rings of PVP chains in the PI/PVP nanoencapsulating layer are expected to scavenge HF, owing to their Lewis basicity^{21,22}. Here, as a supplementary experiment to prove HF-scavenging capability of PI/PVP nanoencapsulating layer, the variation in characteristic XPS peaks (here, focusing on nitrogen atoms) of a PI/PVP (or PI) film was monitored, before/after being swelled with HF (100 ppm)-dissolved liquid electrolyte (1 M LiPF₆ in EC/EMC = 1/2 v/v). To exactly estimate the content of HF trapped by the PI/PVP, physically adsorbed HF and residual LiPF₆ salts in the electrolyte-swollen films were removed with dimethyl carbonate prior to the XPS measurement. The XPS peak corresponding to nitrogen atoms of pyrrolidone rings is broadened after the electrolyte absorption (Figure 2e), indicating that the N-H bonds³¹ are newly formed. This result demonstrates that PI/PVP (specifically, pyrrolidone ring of PVP) effectively scavenges HF dissolved in liquid electrolyte. On the other hand, inappreciable shift of the XPS peak was observed at the liquid electrolyte-swollen PI film (Figure 2f).

The abovementioned multifunctional benefits of the PI/PVP nanoencapsulating layer on the interfacial stability between LCO and liquid electrolyte, with a particular focus on suppressing direct exposure of LCO to liquid electrolyte and also HF-triggered side reactions, are schematically illustrated in Figure 3a.

The effect of PI/PVP nanoencapsulating layer on the interfacial exothermic reaction between the high voltage (4.4 V)-charged LCO and liquid electrolyte was investigated with differential scanning calorimetry (DSC) measurement (Figure 3b). The pristine LCO shows a large exothermic heat ($\Delta H = 706 \text{ J g}^{-1}$) and low exothermic peak temperatures ($T_{\text{peak}} = 217, 245^\circ\text{C}$), revealing vigorous interfacial exothermic reaction between the delithiated LCO and liquid electrolyte. Meanwhile, the PVP-LCO negligibly improves the thermal stability. In comparison, for the PI-LCO, the exothermic heat is reduced and the exothermic peak also shifts to higher temperatures. A notable finding is that the PI/PVP-LCO offers the most stable thermal stability ($\Delta H = 375 \text{ J g}^{-1}$ and $T_{\text{peak}} = 226, 253^\circ\text{C}$) than other LCO samples. These DSC results indicate that the interfacial exothermic reaction between the delithiated LCO and liquid electrolytes is strongly dependent on the coverage area of polymer coating layers. More specifically, the PI/PVP nanoencapsulating layer having highly-continuous surface coverage, as compared to the other polymer layers such as PVP and PI, effectively prevents the direct contact

of LCO surface with liquid electrolyte, thereby alleviating the interfacial exothermic reaction. This advantageous effect of the PI/PVP nanoencapsulating layer on the exothermic reaction at the LCO-electrolyte interface is also conceptually depicted in Figure 3a.

Discussion

The abovementioned in-depth characterization of PI/PVP-LCO demonstrated the potential contribution of PI/PVP semi-IPN conformational nanoencapsulating layer featuring the anomalous multifunctionality as a new class of polymer-based surface engineering to address interfacial issues between cathode materials and liquid electrolytes. The unusual PI/PVP semi-IPN nanoencapsulating layer having large coverage area was successfully formed on LCO surface, owing to its well-tailored polarity matching with LCO. Moreover, the PI/PVP semi-IPN, bearing pyrrolidone rings with Lewis basicity, exhibited the HF-scavenging capability. The combined effects of morphological uniqueness and chemical functionality enabled the PI/PVP semi-IPN nanoencapsulating layer to mitigate direct exposure of LCO to liquid electrolytes and also HF-triggered side reactions. As a result, the PI/PVP-LCO brought the unprecedented improvements in the electrochemical performance and thermal stability of high-voltage charged cells, which lie far beyond those accessible with conventional single component polymer coatings. We believe that the multifunctional PI/PVP semi-IPN nanoencapsulating layer-based surface control strategy can be suggested as a simple and versatile platform technology to stabilize interface between electrode materials and liquid electrolytes, thus facilitating the progress of next-generation high-performance/high-safety lithium-ion batteries.

Methods

Synthesis of PI/PVP semi-IPN-nanoencapsulated LCO powders. A PMDA/ODA (= 1.00/1.01, molar ratio)-based polyamic acid solution was prepared using DMAc as a solvent under nitrogen atmosphere. The detailed synthesis of the polyamic acid was described in previous publications^{32,33}. The polyamic acid solution was then mixed with PVP solution, where the PVP solution was prepared by dissolving PVP powders ($M_w = 55,000 \text{ g mol}^{-1}$, Aldrich) into DMAc. The composition ratio of polyamic acid/PVP was 50/50 w/w and the polymer concentration in the mixture solution was 0.5 wt%. After obtaining the polyamic acid/PVP solution, LCO powders (average particle size = 5 μm , Umicore) were added to the mixture solution and then subjected to ultrasonication for securing uniform dispersion. The polyamic acid/PVP-coated LCO powders are filtered and vacuum-dried at 30°C. In order to convert the polyamic acid into PI, the polyamic acid/PVP-coated LCO powders were thermally cured via a stepwise imidization process under nitrogen atmosphere, leading to formation of PI/PVP-nanoencapsulated LCO powders. The detailed imidization procedure and characterization of the thermally-cured PI were reported in our previous publications^{16–18}. A schematic representation depicting the synthesis procedure of PI/PVP-LCO, along with chemical structures of PVP, PMDA/ODA polyamic acid, and resulting PI, is presented in Figure S1.

Structural/physicochemical characterization of PI/PVP semi-IPN-nanoencapsulated LCO powders and their effect on electrochemical performance/thermal stability of high voltage-charged cells. The surface morphology of PI/PVP-LCO was characterized using field emission scanning electron microscopy (FE-SEM, Hitachi) and transmission electron microscopy (TEM, JEOL). To conduct an in-depth investigation of phase separation behavior of the PI/PVP semi-IPN, a self-standing PI/PVP film as well as single component PI or PVP film was prepared using a conventional casting technique. The glass transition temperatures (T_g) and characteristic FT-IR peaks of the polymer samples were characterized by differential scanning calorimeter (DSC, TA Instruments, heating rate = 10°C min⁻¹) and FT-IR spectrometer (FT-3000, Excalibur), respectively. The polarity of the polymer samples was estimated by measuring their water contact angle using drop shape analyzer (MarkTECH). The LCO cathodes were fabricated by coating NMP-based slurry with a mixture of 95 wt% of LCO, 3 wt% of polyvinylidene fluoride binder, and 2 wt% of carbon black additive on an aluminum current collector (active mass loading = 16 mg cm⁻²). A unit cell (2032-type coin) was assembled by sandwiching a PE separator (thickness = 20 μm , Tonen) between the PI/PVP-LCO cathode and natural graphite anode (graphite/PVdF/carbon black = 90/8/2 w/w/w). The unit cell was then activated by being filled with a liquid electrolyte of 1 M LiPF₆ in ethylene carbonate (EC)/ethyl methyl carbonate (EMC) = 1/2 v/v (Soulbrain). The discharge capacities and C-rate capability were evaluated by varying discharge current densities (i.e., discharge C-rates) from 0.2 (=0.52 mA cm⁻²) to 2.0 C at a constant charge current density of 0.2 C. The cells were cycled at constant charge/discharge current densities of 0.5 C/0.5 C under a voltage range of 3.0–4.4 V. The AC impedance of the



cells was measured using an impedance analyzer (VSP classic, Bio-Logic) over a frequency range from 10^{-3} to 10^6 Hz. The interfacial exothermic reaction between the delithiated LCO and liquid electrolyte was examined by DSC measurements, where the cells were charged to 4.4 V at a current density of 0.1 C and then disassembled in a dry room to remove the charged cathode.

- Armand, M. & Tarascon, J. M. Building better batteries. *Nature* **451**, 652–657 (2008).
- Thackeray, M. M., Wolverton, C. & Isaacs, E. D. Electrical energy storage for transportation—approaching the limits of, and going beyond, lithium-ion batteries. *Energy Environ. Sci.* **5**, 7854–7863 (2012).
- Scrosati, B., Hassoun, J. & Sun, Y. K. Lithium-ion batteries. A look into the future. *Energy Environ. Sci.* **4**, 3287–3295 (2011).
- Manthiram, A. Materials challenges and opportunities of lithium ion batteries. *J. Phys. Chem. Lett.* **2**, 176–184 (2011).
- Whittingham, M. S. Lithium batteries and cathode materials. *Chem. Rev.* **104**, 4271–4301 (2004).
- Goodenough, J. B. & Kim, Y. Challenges for rechargeable Li batteries. *Chem. Mater.* **22**, 587–603 (2010).
- Ellis, B. L., Lee, K. T. & Nazar, L. F. Positive electrode materials for Li-ion and Li-batteries. *Chem. Mater.* **22**, 691–714 (2010).
- Xu, K. Nonaqueous liquid electrolytes for lithium-based rechargeable batteries. *Chem. Rev.* **104**, 4303–4417 (2004).
- Zhang, S. S. A review on electrolyte additives for lithium-ion batteries. *J. Power Sources* **162**, 1379–1394 (2006).
- Cho, J. P., Kim, Y. J. & Park, B. W. Novel LiCoO₂ cathode material with Al₂O₃ coating for a Li ion cell. *Chem. Mater.* **12**, 3788–3791 (2000).
- Hwang, B. J. *et al.* Mechanism study of enhanced electrochemical performance of ZrO₂-coated LiCoO₂ in high voltage region. *J. Power Sources* **195**, 4255–4265 (2010).
- Sun, Y. K. *et al.* AlF₃-coating to improve high voltage cycling performance of Li[Ni_{1/3}Co_{1/3}Mn_{1/3}]O₂ cathode materials for lithium secondary batteries. *J. Electrochem. Soc.* **154**, A168–A172 (2007).
- Lepage, C. *et al.* A soft chemistry approach to coating of LiFePO₄ with a conducting polymer. *Angew. Chem., Int. Ed.* **50**, 6884–6887 (2011).
- Dinh, H. C. *et al.* Electrochemical analysis of conductive polymer-coated LiFePO₄ nanocrystalline cathodes with controlled morphology. *Electroanalysis* **23**, 2079–2086 (2011).
- Abouimrane, A. *et al.* 3-Hexylthiophene as a stabilizing additive for high voltage cathodes in lithium-ion batteries. *J. Electrochem. Soc.* **160**, A268–A271 (2013).
- Park, J. H. *et al.* A novel ion-conductive protection skin based on polyimide gel polymer electrolyte: application to nanoscale coating layer of high voltage LiNi_{1/3}Co_{1/3}Mn_{1/3}O₂ cathode materials for lithium-ion batteries. *J. Mater. Chem.* **22**, 12574–12581 (2012).
- Park, J. H. *et al.* Polyimide gel polymer electrolyte-nanoencapsulated LiCoO₂ cathode materials for high-voltage Li-ion batteries. *Electrochem. Commun.* **12**, 1099–1102 (2010).
- Cho, J. H. *et al.* A polymer electrolyte-skinned active material strategy toward high-voltage lithium ion batteries: a polyimide-coated LiNi_{0.5}Mn_{1.5}O₄ spinel cathode material case. *Energy Environ. Sci.* **5**, 7124–7131 (2012).
- Kwon, Y. H., Kim, S. C. & Lee, S. Y. Nanoscale phase separation of sulfonated poly(arylene ether sulfone)/poly(ether sulfone) semi-IPNs for DMFC membrane applications. *Macromolecules* **42**, 5244–5250 (2009).
- Ha, H. J. *et al.* UV-curable semi-interpenetrating polymer network-integrated, highly bendable plastic crystal composite electrolytes for shape-conformable all-solid-state lithium ion batteries. *Energy Environ. Sci.* **5**, 6491–6499 (2012).
- Oster, G. & Immergut, E. H. Ultraviolet and infrared spectral studies of polyvinylpyrrolidone. *J. Am. Chem. Soc.* **76**, 1393–1396 (1954).
- Gupta, A. *et al.* Porous Nylon-6 fibers via a novel salt-induced electrospinning method. *Macromolecules* **42**, 709–715 (2009).
- Palacin, M. R. Recent advances in rechargeable battery materials: a chemist's perspective. *Chem. Soc. Rev.* **38**, 2565–2575 (2009).
- Kushida, K. & Kuriyama, K. Sol-gel growth of LiCoO₂ films on Si substrates by a spin-coating method. *J. Cryst. Growth* **237–239**, 612–615 (2002).
- Kim, Y. K., Park, H. B. & Lee, Y. M. Carbon molecular sieve membranes derived from thermally labile polymer containing blend polymers and their gas separation properties. *J. Membr. Sci.* **243**, 9–17 (2004).
- Oh, T. J., Nam, J. H. & Jung, Y. M. Molecular miscible blend of poly(2-cyano-1,4-phenyleneterephthalamide) and polyvinylpyrrolidone characterized by two-dimensional correlation FTIR and solid state ¹³C NMR spectroscopy. *Vib. Spectrosc.* **51**, 15–21 (2009).
- Chen, Z. & Dahn, J. R. Methods to obtain excellent capacity retention in LiCoO₂ cycled to 4.5 V. *Electrochim. Acta* **49**, 1079–1090 (2004).
- Kim, Y. J., Cho, J., Kim, T. J. & Park, B. Suppression of cobalt dissolution from the LiCoO₂ cathodes with various metal-oxide coatings. *J. Electrochem. Soc.* **150**, A1723–A1725 (2003).
- Liu, G. Q. & Kuo, H. T. Study of electrochemical properties of coating ZrO₂ on LiCoO₂. *J. Alloys Comp.* **496**, 512–516 (2010).
- Lux, S. F. *et al.* The mechanism of HF formation in LiPF₆ based organic carbonate electrolytes. *Electrochem. Commun.* **14**, 47–50 (2012).
- Graf, N. *et al.* XPS and NEXAFS studies of aliphatic and aromatic amine species on functionalized surfaces. *Surf. Sci.* **603**, 2849–2860 (2009).
- Choi, M. C., Kim, Y. K. & Ha, C. S. Polymers for flexible displays: From material selection to device applications. *Prog. Polym. Sci.* **33**, 581–630 (2008).
- Graf, N., Zhu, H. & Liu, T. In situ thermal preparation of polyimide nanocomposite films containing functionalized graphene sheets. *ACS Appl. Mater. Interfaces* **2**, 3702–3708 (2010).

Acknowledgments

This research was supported by the MSIP (Ministry of Science, ICT & Future Planning), Korea, under the C-ITRC (Convergence Information Technology Research Center) support program (NIPA-2013-H0301-13-1009) supervised by the NIPA (National IT Industry Promotion Agency). This work was also supported by Energy Efficiency and Resources R&D program (20112010100150) under the Ministry of Knowledge Economy, Republic of Korea. This study was also supported by the BK21 Plus funded by the Ministry of Education, Korea (10Z20130011057).

Author contributions

J.K. designed the experiments and prepared the samples and cathode fabrications, characterizations and tests. J.P. performed the electrochemical analysis. C.L. participated in characterizing and discussing the phase separation behavior. S.L. commented on the experimental results and wrote the main manuscript text. All authors discussed the results and reviewed the manuscript.

Additional information

Supplementary information accompanies this paper at <http://www.nature.com/scientificreports>

Competing financial interests: The authors declare no competing financial interests.

How to cite this article: Kim, J.-M., Park, J.-H., Lee, C.K. & Lee, S.-Y. Multifunctional semi-interpenetrating polymer network-nanoencapsulated cathode materials for high-performance lithium-ion batteries. *Sci. Rep.* **4**, 4602; DOI:10.1038/srep04602 (2014).



This work is licensed under a Creative Commons Attribution-NonCommercial-NoDerivs 3.0 Unported License. The images in this article are included in the article's Creative Commons license, unless indicated otherwise in the image credit; if the image is not included under the Creative Commons license, users will need to obtain permission from the license holder in order to reproduce the image. To view a copy of this license, visit <http://creativecommons.org/licenses/by-nc-nd/3.0/>